Plasma-Introduced Oxygen Defects Confined in $Li_4Ti_5O_{12}$ Nanosheets for Boosting Lithium-ion diffusion

Jianfeng Zhu[1], Jian Chen[1,*], Hui Xu[1], Shangqi Sun[1], Yang Xu[2], Min Zhou[1*], Xue Gao[1], Zhengming Sun[1]

1. Jiangsu Key Laboratory of Advanced Metallic Materials, School of Materials Science and Engineering, Southeast University, Nanjing, 211189, China

2. Department of Chemistry, University College London, 20 Gordon Street, London WC1H 0AJ, UK.

Corresponding authors

*E-mail: j.chen@seu.edu.cn.
*E-mail: min.zhou@tu-ilmenau.de.

Key words:

$Li_4Ti_5O_{12}$; Oxygen vacancy; Li-ion diffusion coefficient; Plasma; Li-ion battery;

Abstract

Although $Li_4Ti_5O_{12}$ (LTO) is considered as promising anode material for high-power Li-ion battery with high safety, the sluggish Li-ion diffusion coefficient restricts its wide application. In this work, oxygen vacancy was successfully incorporated into LTO by an eco-friendly and cost-effective plasma process. The deficient LTO delivers much higher capacity of 173.4 mAh g^{-1} at 1 C rate after 100 cycles and 140.5 mAh g^{-1} at 5 C after 1000 cycles than those of the pristine LTO. Meanwhile, even at high rate of 20 C it displays an ultrahigh capacity of 133.1 mAh g^{-1} after 500 cycles with a Coulombic efficiency of 100%. Detailed analysis discovers that the lithium storage mechanisms in the oxygen-deficient LTO, especially at high rate, were dominated by the insertion behavior and dual-phases conversion due to the fast ion diffusion ability, rather than the widely reported surface capacitance by other approaches. This work highlights that the defect generation by plasma in nanomaterials is an effective way to promote the ion mobility, especially at high rate, thus can be extended to other electrode materials for advanced energy-storage applications.

1. Introduction

Electrochemical energy storage is of intensive interest to meet the increasing demands of electronic devices, vehicles and renewable energy commercialization. Among various techniques, lithium-ion batteries (LIBs) have not only dominated portable energy storage, but also attracted continuous research interests in pursuit of higher charge capacity and rate capability for upcoming large-scale applications. In general, the lithium storage ability strongly depends on the properties of electrode materials, and thus corresponding studies, especially of anode materials, stand out as the research core recently.[1-2] Carbon-based materials have been widely used for commercial anodes, but suffer from large volume expansion and shrinkage during Li-ion intercalation/extraction and safety concerns owing to the lithium dendrite formation at low Li-ion intercalation potential. Therefore, it is significant to develop other alternative anodes.[3-7]

The spinel $Li_4Ti_5O_{12}$ (LTO) has attracted wide attention as a potential intercalation-type anode candidate with long cycling stability and high safety. The preeminent performance is ascribed by a negligible volume change (often called as 'zero-strain') during the Li-ion insertion/extraction accompanied with one-electron transfer of Ti^{4+} and Ti^{3+} redox. A LTO lattice cell can accommodate three Li-ions with a theoretical specific capacity of 175 mAh g^{-1} at comparatively high flat potential of 1.55 V, thus avoiding the formation of dendrites. Despite these superiorities, the rate capabilities of LTO are unsatisfactory due to the poor Li-ion diffusion coefficient (~10^{-13} cm^2 s^{-1}).[8-11] Various strategies have been proposed to improve the Li-ion diffusion of LTO, including reducing the particle size, doping heteroatoms (including cations and anions), fabricating distinctive nanostructure, coating carbon and other materials.[12-18] In an attempt to overcome this challenge, the first question that arises is the origin of capacities at different rates, which may come from bulk (insertion/extraction) or surface (pseudocapacitance or double-layer capacitance), as different mechanisms require distinguishing strategies for optimizing Li-ion diffusion.[19-23]

Introducing oxygen vacancies (OVs) has been proved as an efficient strategy to improve the capacities at high rates with the contributions of enhancing bulk capacities [19-20] and surface capacitances [21-24]. The preparation of the OVs is usually realized by thermal treatments in reducing atmosphere and hydrothermal synthesis with discreet controls. However, these processes usually require long time and high energy consumption, and even with chemical pollution. Plasma treatments provide one promising option to circumvent these problems as an eco-friendly and energy-saving alternative to existing processes. In addition, plasma is ionized gas and contains charged particles with high kinetic energy, showing powers to functionalize, tailor and fabricate surfaces and nanomaterials.[25-27]

With the interaction between the active particles in plasma and the bombarded subjects, it has been found that OVs can be effectively created in many anode materials such as Co_3O_4, TiO_2 and MoS_2.[28-30] For example, He *et al* [31] synthesized oxygen-deficient TiO_2 in Ar/H_2 plasma, which exhibited improved electrochemical performance. In addition, the OVs by plasma bombardment can boost the sodium-ion storage of TiO_2 as reported by Gan *et al* [32] owing to the improved ion diffusion coefficient and possible surface pseudocapacity process. Within the knowledge of the authors, there are few studies on plasma effects on LTO. Lan *et al* [33] only treated the as-fabricated electrode (the mixture of LTO, conductive carbon and binder) by atmospheric pressure plasma in Ar/N_2 and achieved improved capacity (132 mAh g^{-1}) and stability for 100 cycles at 10 C by the presence of OVs. Clearly the plasma effects on $Li_4Ti_5O_{12}$ as well as the storage mechanisms of introduced OVs, especially the Li-ion mobility at high rate, need be further explored.

Herein, the as-synthesized LTO nanosheets were treated by plasma process in a reducing atmosphere to produce oxygen defects in the spinel lattice. In comparison with the pristine LTO, the plasma-treated LTO (PLTO) shows significantly improved electrochemical energy storage with ultrahigh specific capacity (173.4 mAh g^{-1} at 1 C after 100 cycles), and remarkable rate capacity (133.1 mAh g^{-1} at 20 C after 500 cycles), which are 18% and 48% higher than those of the LTO, respectively. The electrochemical analysis fully evidence that the lithium storage of LTO nanosheets are diffusion-controlled mechanism rather than a capacitive process-dominated mechanism, even at the high rate of 5 C. Hence, introducing OVs by plasma into LTO to improve Li-ion diffusion in bulk is an effective strategy to deliver a high rate-performance. This study offers the highly efficient approach for targeted design for performance enhancement, and provides a new insight into the influence of plasma modulated OVs for intercalation-type anode materials.

2.Experimental

2.1 Material Synthesis

$Li_4Ti_5O_{12}$ nanosheets were synthesized through a facile strategy. In detail, 20 mM tetrabutyl titanate was added into 40 mL of anhydrous ethanol, fully stirring for 30 min. Meanwhile 18.4 mM $LiOH•H_2O$ was dissolved into 40 mL of deionized water with complete dissolution. Then, the LiOH solution was dropwise added into the tetrabutyl titanate ethanol solution with vigorously stirring. The mixture was stirred for 2 h to fully mix the components. Subsequently, the solution was transferred to a 100 mL Teflon-lined autoclave, then heated at 180 ºC for 24 h. after cooled down to room temperature, the precipitates were centrifuged and washed with ultrapure water and ethanol, and then dried at 60 ºC for 12 h. Finally the obtained precursor was calcined at 600 ºC for 6 h in air. The $Li_4Ti_5O_{12}$ nanosheets were obtained.

2.2 Plasma Treatment

The deficient LTO nanosheets were prepared by treating the LTO precursor in a H_2/N_2 (the flow rate of H_2 and N_2 were both 100 sccm) plasma atmosphere. The process maintained at the pressure of 5 Pa and temperature of 150 ºC for 2 h.

2.3 Material Characterization

Phase analysis of as-prepared samples were initially characterized by X-ray diffraction (XRD) using an X-ray diffraction analyzer with Cu-Kα eradiation (D8-Discover, Bruker). The morphology and microstructure of samples were analyzed using a field emission scanning electron microscope (FESEM, Sirion, FEI) and a high-resolution transmission electron microscope (HRTEM, Tecnai F20, FEI). The electronic state of samples were investigated by X-ray photoelectron spectroscopy (XPS) using a VG MultiLab 2000 system with a monochromatic Al Kα X-ray source (Thermo VG Scientific). The transmittance spectra of the anode materials were recorded using a diffuse reflectance UV-VIS spectroscopy with wavelength from 200 to 800 nm. Raman (Thermo Fisher DXRxi) measurement was conducted with a laser wavelength of 532 nm.

2.4 Electrochemical Measurements

The electrochemical performance of materials was examined using a CR2032-type coin cell assembled in an Ar-filled glove box. The working electrodes were prepared by evenly mixing the $Li_4Ti_5O_{12}$, super P and polyvinylidene difluoride (PVDF) in a weight ratio of 75:15:10. The uniform slurry was coated onto a pure Cu foil and dried at 80 ºC for 12 h under vacuum. The working electrodes were punched into 13 mm diameter circular disks with an active-material loading of ~1.2 mg cm^{-2}. Pure lithium foil was used as the counter electrode and the Celgard 2400 was used as the separator. The 1M solution of $LiPF_6$ in ethylene carbonate and dimethyl carbonate (EC+DMC,1:1) was used as electrolyte. The galvanostatic charge/discharge measurements were implemented using a LAND battery test system in the voltage range of 1.0 to 2.5 V (vs. Li/Li^+) at different current densities. The cyclic voltammetry (CV) and electrochemical impedance spectroscopy (EIS) measurements were performed using a CHI660e electrochemical station. The EIS measurement was conducted in the frequency range of 0.1 Hz to 100 kHz at the open circuit voltage.

3. Results and discussion

3.1 Microstructure and phase constituents

The as-synthesized LTO by the hydrothermal fabrication was treated by plasma process at 150 ºC in a mixture of hydrogen and nitrogen atmosphere (denoted as PLTO) as demonstrated in **Figure S1.** The SEM images in **Figure 1a&1b** show that both samples display similar nanosheet features, but the PLTO possesses smaller size due to the etching effects originating from the sputtering effects of the energetic particles in plasma. The particle size distribution curves of the two samples also confirm the reduced size of PLTO, as shown in **Figure S2**. The XRD patterns of both samples in **Figure 1c** show clear diffraction peaks indexed to cubic spinel LTO (JCPDS No. 49-0207) with trace amount of anatase TiO_2 (JCPDS No. 21-1272) and rutile TiO_2 (JCPDS No. 21-1276).[34-36] Rietveld refinement analysis in **Figure 1d&1e** indicates that the phase constituents were similar and negligibly affected.

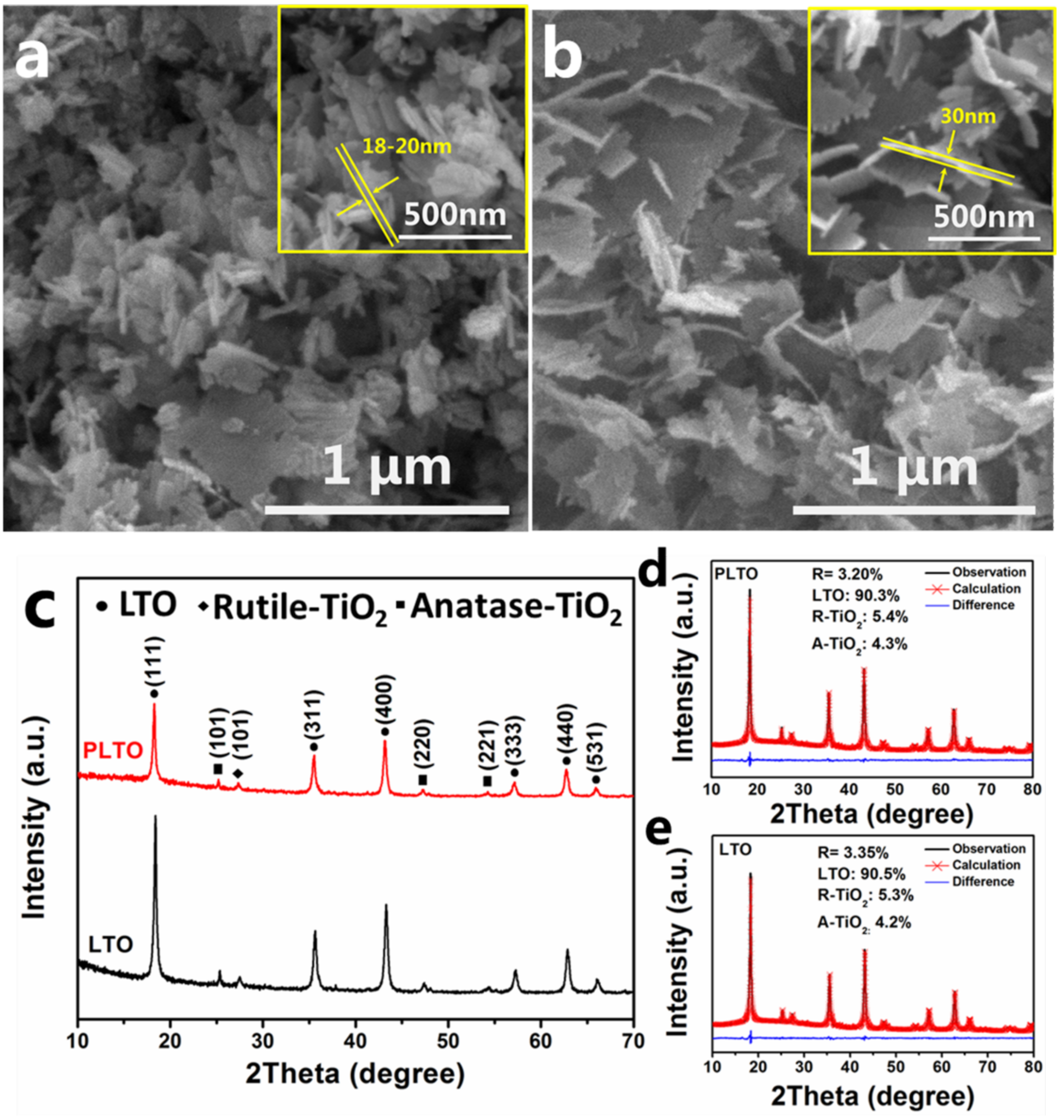

Figure 1. SEM images of (a) PLTO and (b) LTO, (c) XRD patterns of LTO and PLTO, (d) Rietveld refinement analysis for XRD patterns of PLTO and (e) LTO.

3.2 Oxygen vacancies

Notwithstanding, magnified diffraction peaks of (111) and (400) in **Figure 2a&2b** show clear shifts to lower diffraction angles due to the lattice expansion (~1%) after the plasma treatment. Meanwhile, the lattice expansion of plane (111) was also observed in HRTEM in **Figure 2c&2d**. This can be attributed to the formed defects in the lattice, especially the OVs, by bombardments of energetic particles in plasma, leading to the partial reduction of Ti^{4+} ions to larger Ti^{3+} ions to maintain the charge neutrality. The expanded latteic may facilitate the ion diffusion and is beneficial for improved electrochemical performance.[37-39]

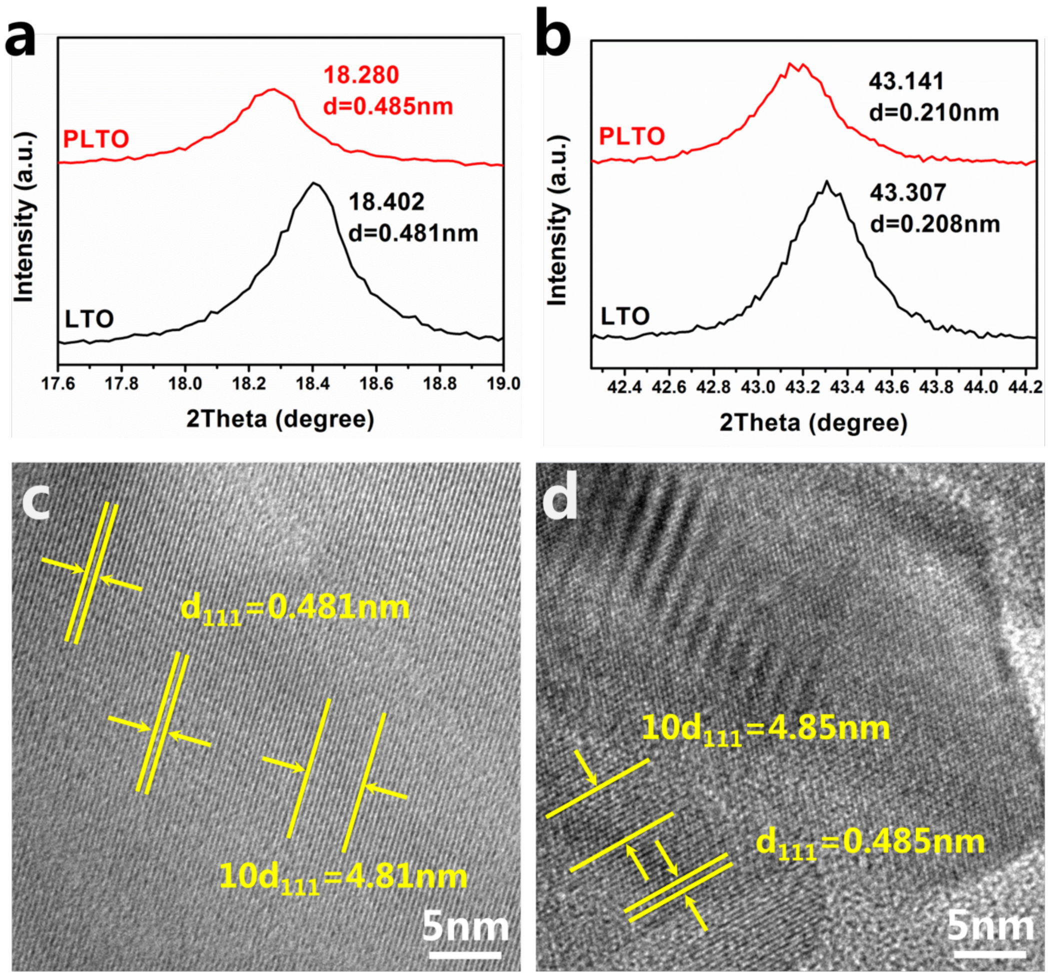

Figure 2. Enlarged XRD patterns of (a) the (111) diffraction peak and (b) the (400) diffraction peak. HRTEM images of (c) LTO and (d) PLTO.

In order to confirm the existence of OVs, the surface chemical states of both samples were investigated by X-ray photoelectron spectroscopy (XPS) in **Figure 3** and **Figure S3**. **Figure 3a&3b** show the fitting curves of O 1s spectra that are decomposed into three peaks, locating at 529.5, 532.3 and 531.6 eV corresponding to the Ti-O bonds, the hydroxyl species of surface-adsorbed water molecules, and the defects with low oxygen coordination, respectively.[30, 40-41] The peak area at 531.6 eV for PLTO is 11.59 % greater than that of LTO (8.02%), indicating more OVs. Compared to those of LTO, the Ti 2p peaks of PLTO shifted to the lower binding energy, from 458.4 and 464.1 eV to 458.0 and 463.9 eV respectively. Meanwhile, the fitted peak for Ti^{3+} is shown in **Figure S3c & 3d**. It can be clearly observed that PLTO possesses more Ti^{3+} (13.77%) than LTO (6.94%) after the introduction of OVs. The conversion of Ti from +4 to +3 valence state always companies with the formation of oxygen vacancy for the overall charge balance.[42-44]

Electron paramagnetic resonance (EPR) results further consolidate the existence of OVs. As shown in **Figure 3c**, there is a high signal of *g* at 2.003 in PLTO which originates from the unpaired electrons trapped in OVs. Meanwhile, the existence of Ti^{3+} is also confirmed by EPR signal at *g*=1.945 assigned to Ti^{3+} in **Figure S4**.[31, 45-47] The variation of bandgap evidenced by UV-vis DRS spectra in **Figure 3d** and the blue-shifted Ti-O Raman peaks for PLTO in **Figure S5** also agree with the existence of OVs.[48-49]

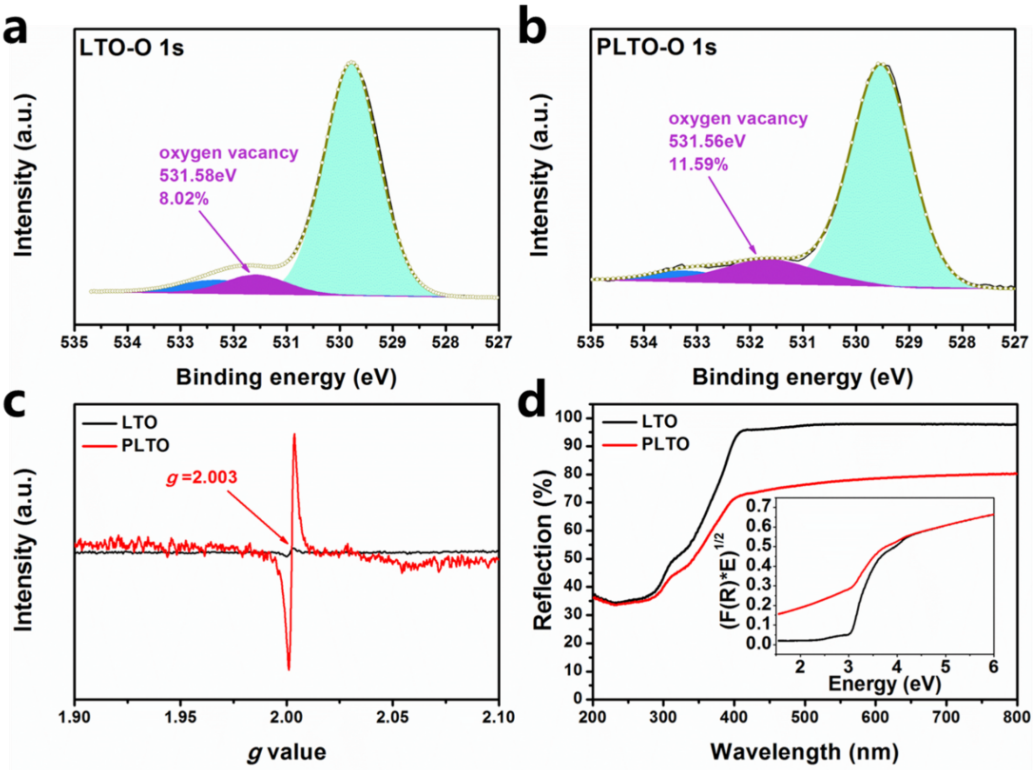

Figure 3. High resolution of O 1s XPS spectra of (a) LTO and (b) PLTO, (c) EPR spectra and (d) UV-vis DRS spectra of LTO and PLTO.

3.3 Electrochemical performance

Figure 4a displays the first CV cycles of LTO and PLTO at 0.1 mV s^{-1}, in which both samples show a pair of redox peaks at ~1.5 V/~1.65 V, corresponding to the Li-ion insertion/desertion in $Li_4Ti_5O_{12}$.[50-51] The PLTO shows lower polarization according to the voltage difference between the anodic and cathodic peaks (~210 mV) and higher peak currents. Moreover, the CV curves for 1st, 2nd and 3rd cycles in **Figure S6**show the PLTO presented smaller polarization than LTO, suggesting its better electrochemical kinetics. **Figure 4b** shows the galvanostatic charge-discharge cycling results at 1 C (175 mAh g^{-1}). In comparison with pristine LTO, PLTO exhibited the superior specific capacity of 173.4 mAh g^{-1} after 100 cycles. The rate capability in **Figure 4c** was 180.7, 177.8, 171.9, 170.4, 160 and 149.7 mAh g^{-1} at 1, 2, 5, 10, 20 and 30 C, respectively. When the rate returned 1 C, the discharge capacity recovered to ~177.8 mAh g^{-1}, which was slightly higher than the theoretic value of $Li_4Ti_5O_{12}$. Considering similar morphology features and other measurement parameters, the extraordinary capacity of PLTO may be attributed to the existence of OVs which can act as extra Li^+ trapping sites during the electrochemical process.[52-55]

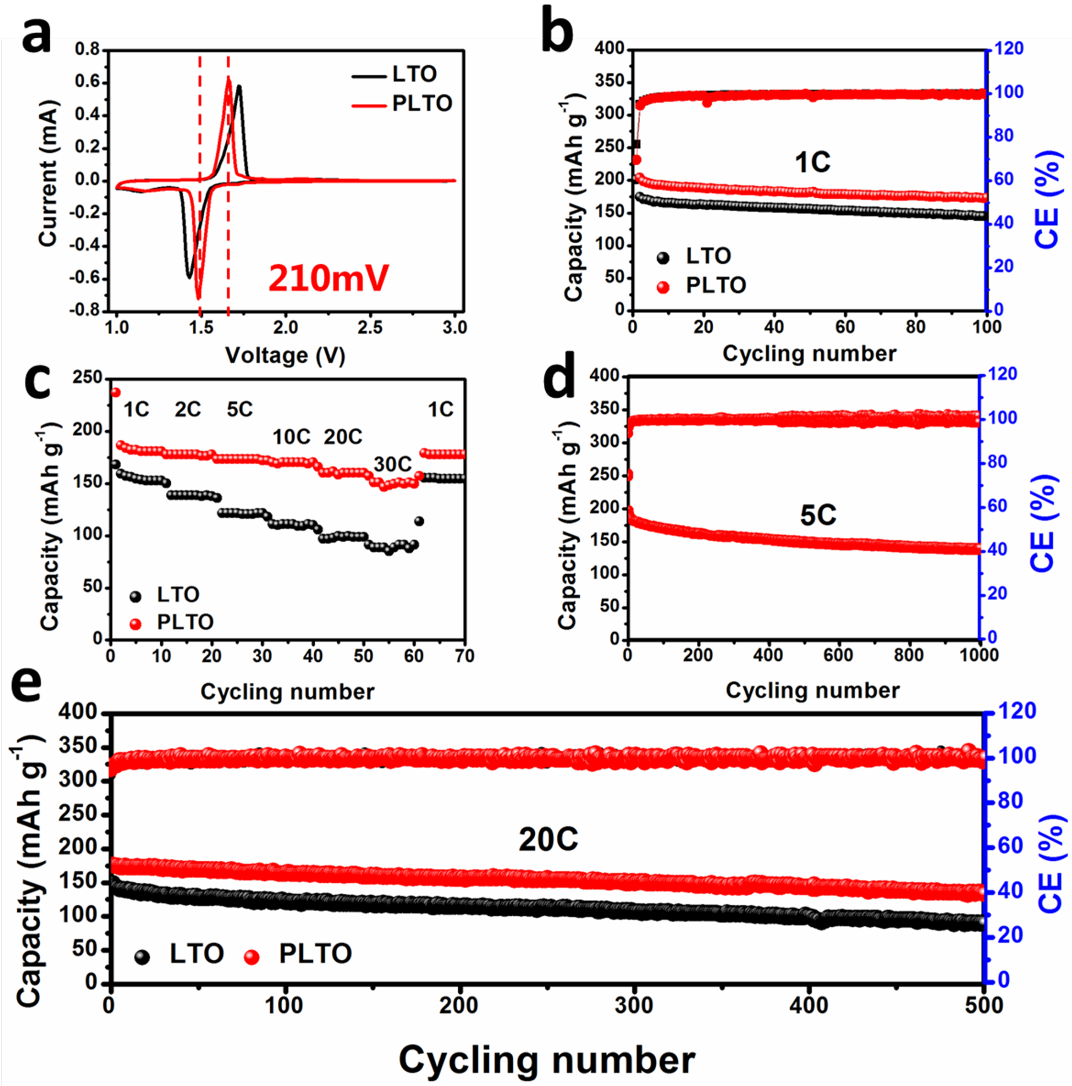

Figure 4. (a) The first cycle of CV curves of LTO and PLTO at 0.1mV s^{-1}, (b) cycling performance of LTO and PLTO at 1 C, (c) rate performance of LTO and PLTO, (d) cycling performance of LTO and PLTO at 5 C, (e) cycling performance of PLTO at 20 C.

The long-term stability at high rates in **Figure 4d&4e**. At the rate of 20 C, a high capacity of 133.1 mAh g^{-1} can be reached for PLTO after 500 cycles, whereas the LTO exhibited a capacity of only 90.4 mAh g^{-1}. At 5 C, PLTO delivered a high capacity of 140.5 mAh g^{-1} at 5 C after 1000 cycles, with a CE of ~100%. The initial CE of PLTO at 20 C and 5 C were 95.03% and 74.07% respectively. The relatively low initial CE of PLTO is ascribed to the absorbed trace water and surface defects as a common phenomenon of nanomaterials.[50] In comparison with the pristine LTO, the specific capacity has been increased by 18% and 48% respectively indicating that the introduced OVs can greatly boost the kinetic properties of $Li_4Ti_5O_{12}$.[56] Meanwhile, the comparison of the electrochemical performance of the PLTO with the reported electrodes is shown in **Table S2** and the PLTO shows significantly improved performance.

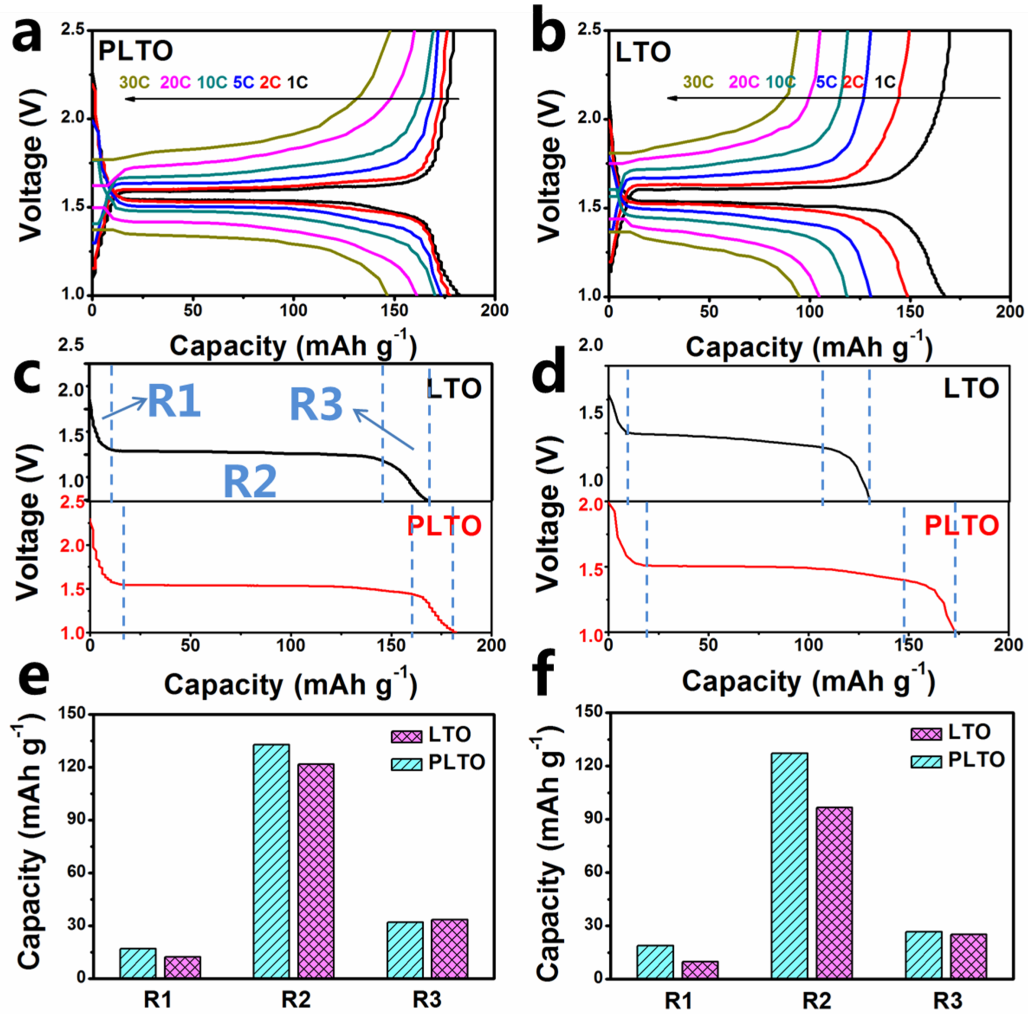

Figure 5. Discharge/charge curves of (a) PLTO and (b) LTO at various rates from 1 C to 30 C, discharge curves of LTO and PLTO at (c) 1 C and (d) 5 C, corresponding capacity contributions of different regions for LTO and PLTO at (e) 1 C and (f) 5 C.

Since the origin of capacities at different rates is important to understand the detailed influences of OVs, the charge/discharge curves of LTO and PLTO at different rates are further investigated to visualize the detailed contributions of different storage mechanism. **Figure 5a&5b** show the improved electrochemical performance of PLTO with higher specific capacities and less polarization than that of LTO in consistent with the CV results.[57-58] **Figure 5c&5d** compare the discharge curves of LTO and PLTO at 1 C and 5 C which can be separated into three voltage regions: the decreasing voltage region from the open-circle voltage to ~1.55 V (denoted as R1), the plateau at ~1.55 V (denoted as R2) and a sloping region from ~1.55 to 1 V (denoted as R3). The R1 is related to the Li-ion insertion into the $Li_4Ti_5O_{12}$ bulk by the formation of a solid solution domain. The R2 displays a dual-phase conversion region where $Li_4Ti_5O_{12}$ converts to $Li_7Ti_5O_{12}$, and the R3 is considered as the interfacial Li-ion storage in the solid-liquid and the solid-solid interface.[35, 43, 59-61]

As presented in **Figure 5e&5f**, the increased capacity of PLTO was mainly introduced by the Li-ion stored through insertion in Region R1 and the phase transition in Region R2, which belong to the contribution of bulk storage. At Region R1, the contributed capacity for PLTO and LTO were 17.1 and 12.3 mAh g^{-1} at 1 C, respectively. At 5 C, the PLTO displayed more significant contribution from R1 almost double of LTO (18.8 mAh g^{-1} vs 9.8 mAh g^{-1}). At Region R2, the contributed capacities of PLTO were also higher, especially at the high rate at which the enhanced capacity reached 30%. In contrast, the contributed capacities of R3 are much lower and display negligible difference between LTO and PLTO, indicating interfacial capacity has much less contribution than the bulk capacity that is different from the dominant pseudocapacitive effects of OVs using non-plasma processes.[28, 57, 62-63]

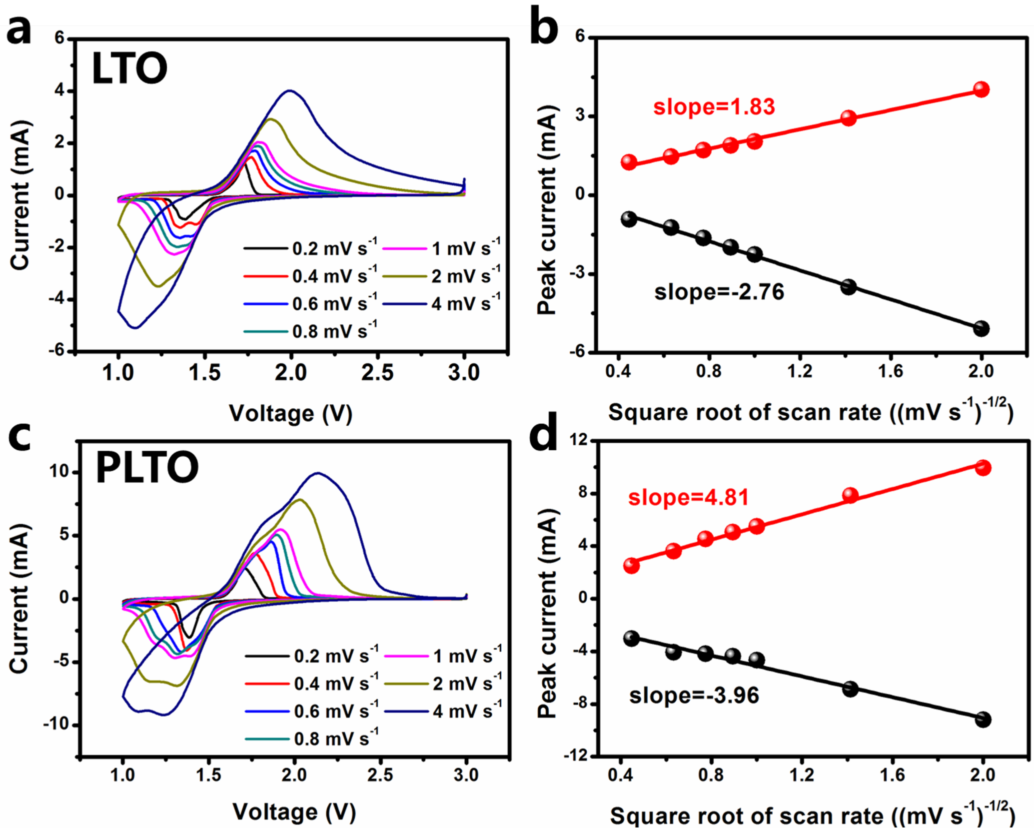

Figure 6. CV curves of (a) LTO and (c) PLTO at different rates from 0.2 mV s^{-1} to 4 mV s^{-1}, corresponding linear relationship between peak current and square root of scan rate of (b) LTO and (d) PLTO.

To confirm our hypothesis, cyclic voltammetry (CV) measurements at various sweep rates from 0.2 to 4 mV s^{-1} of LTO and PLTO were performed. It has been found that the redox peak current i_p increased with the increase of square root of sweep rate v with a linear relationship as presented in **Figure 6b&6d**, indicating that the charging mechanism was dominated by the lithium ion diffusion.[40, 54, 63-65] The diffusion coefficient (D_{Li}) of lithium ion is calculated by the Randles-Sevcik equation:[48, 66-67]

$$i_p = (2.69 \times 10^5)\, n^{3/2} A D_{Li}^{1/2} C_{Li} v^{1/2} \qquad \text{Equation 1}$$

where n is the number of electrons involved in the electrode reaction, A is the area, C_{Li} is the concentration of lithium ions. The D_{Li} of lithiation and delithiation for PLTO are 4.85×10^{-7} and 3.29×10^{-7} $cm^2\ s^{-1}$ respectively, about one order higher than those of LTO (7.03×10^{-8} $cm^2\ s^{-1}$ and 1.59×10^{-8} $cm^2\ s^{-1}$).

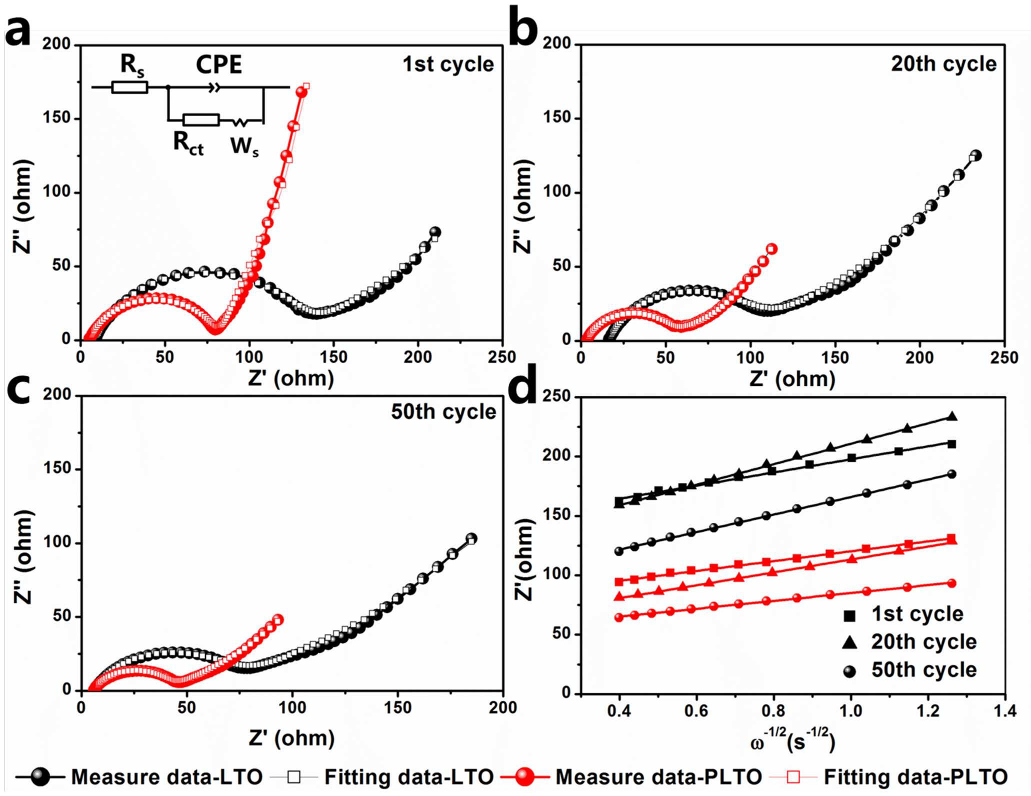

Figure 7. Electrochemical impedance spectra of LTO and PLTO measured after (a) 1st cycle, (b) 20th cycle, (c) 50th cycle, (d) Z' *vs* $\omega^{-1/2}$ at low frequency regions.

Electrochemical impedance spectra measurements (EIS) in **Figure 7** were also performed to study the improved electrochemical performance. All the spectra were composed of a semicircle in the high- and medium-frequency range followed by a straight line at low frequency.[50, 68-70] The PLTO prior to cycling possessed lower charge-transfer resistance (R_{ct}) (77.82 Ω) than that of LTO (124.62 Ω). Even after 20 cycles (**Figure 7b**) and 50 cycles (**Figure 7c**), the PLTO still displayed lower R_{ct} as listed in **Table S1**, indicating that the charge transfer kinetic was significantly improved by introduction of OVs. The charge-transfer resistance displays a decreasing trend with the increase of the cycles as demonstrated in **Figure 7** which can be ascribed by that the irreversible lithium insertion into the oxygen vacancy sites and grain boundaries in electrodes during activation process can increase the conductivity and also the enhanced wetting performance between electrode and electrolyte.[71-73]

The diffusion coefficient D_{Li} of Li-ion in bulk material can be also evaluated by Equation 2:[50, 74]

$$D_{Li} = R^2T^2/2A^2n^4F^4C^2\sigma^2 \qquad \text{Equation 2}$$

where R, T, F, A and C are the gas constant, the absolute temperature, the Faraday's constant, the apparent area of the electrode and the molar concentration of Li-ions, respectively. The values of σ can be obtained from the slopes of the lines in the graph of Z' *vs* $\omega^{-1/2}$. As listed in Table S1, the PLTO also processed higher diffusion coefficient than that of LTO (~2-3 times), in agreement with the CV results.

Based upon, the plasma introduced OVs in LTO possess enhanced Li-ion diffusion coefficients by the CV and EIS measurements, leading to the improved superior electrochemical properties at high rates. As shown in **Figure 5e&5f**, the main contribution to the specific capacity of PLTO and LTO was the lithium insertion reaction and dual-phase conversion, corresponding to the region 1 and region 2 in **Figure 5c&5d**. The interfacial storage ability of the two samples shows almost negligible change. Moreover, when the rate increased to 5C, the capacities of both samples in region 3 were nearly the same with the capacities in region 3 at low rates, while the gap of the whole capacities at different rates result from the different contributions in region 1 and 2. This result indicated that the lithium storage mechanism of PLTO at high rates was still dominated by the lithium insertion and dual-phase conversion behavior. It is worth noting that the introduced OVs by many other approaches (*e.g.* thermal treatment and hydrothermal synthesis) are often accompanied with appreciable pseudocapacity effects [21-22] where charge storage occurs via Faradaic charge transfer at or near the surface of the material. The plasma process, therefore, offers a targeting approach to enhance the Li-ion diffusion of the LTO nanosheets. Through the bombardment by energetic particles in plasma, the lattice constant can be enlarged due to the synergistic effects of the defects and chemical variation as evidenced by the XRD and TEM analysis. In addition, the recent study [65, 75] demonstrates that the enhancement of Li-ion diffusion coefficient may be attributed to the local built-inside electric field originated from the unbalanced charge distribution around the OVs.[76-77] Thus, the oxygen defects introduced by plasma significantly enhanced the electrochemical performance of $Li_4Ti_5O_{12}$ by boosting the Li-ion diffusion. Although oxygen vacancies (OVs) can significantly improve the electrochemical performance, it is a great challenge to stabilize the OVs especially under oxidizing conditions in which the OVs are very active. Within the knowledge of the authors, there are limited stabilizing strategies including the oxygen deficient atmosphere, heteroatom doping, the specific crystalline plane and the interfacial strain. Clearly, it is of great importance to understand the working mechanisms and evolution of OVs in electrochemical systems and more work need be carried out in this field.

4. Conclusion

In summary, this work brought forward a facile, low temperature, eco-friendly and cost-effective plasma approach to generate structural defects to improve the electrochemical properties of $Li_4Ti_5O_{12}$. Benefiting from the introduction of oxygen vacancies, the PLTO exhibited not only high lithium storage ability (a high capacity of 173.4 mAh g^{-1} at 1 C) but also impressive rate capacity (133.1 mAh g^{-1} after 500 cycles at 20 C with a Coulombic efficiency of 100%). The lithium storage mechanisms in the oxygen-deficient PLTO, especially at high rate, were dominated by the insertion behavior and dual-phases conversion due to the fast ion diffusion ability. Such results suggest that the defect generation by plasma in nanomaterials is an effective way to promote the ion mobility, especially at high rate, thus can be extended to other electrode materials for advanced energy-storage applications.

Supporting information

Supporting Information is available from the ACS Online Library or from the author.

Schematic of plasma treatment; Particle size distribution curves of PLTO and LTO; (a) XPS spectra of LTO and PLTO, (b) high solution of Ti 2p XPS spectra of LTO and PLTO, (c) Ti 2p fitted spectra of LTO, (d) Ti 2p fitted spectra of PLTO. EPR spectra of LTO and PLTO; Raman spectra of LTO and PLTO; The CV curves of PLTO and

LTO for 1st, 2nd and 3rd cycles; The R_{ct} value of LTO and PLTO; The elements obtained from the fitting EIS data; Comparison of the electrochemical performance of the plasma-treated LTO with the reported LTO electrodes.

Acknowledgements

This research was supported by the National Natural Science Foundation of China (11472080 and 51731004), Postgraduate Research＆Practice Innovation Program of Jiangsu Province (SJCX18_0033).

Conflict of Interest

The authors declare no conflict of interest.

References

(1) Zheng, S.; Li, X.; Yan, B.; Hu, Q.; Xu, Y.; Xiao, X.; Xue, H.; Pang, H. Transition-Metal (Fe, Co, Ni) Based Metal-Organic Frameworks for Electrochemical Energy Storage. *Advanced Energy Materials* **2017,** *7*, 1602733.
(2) Liu, J.; Bao, Z.; Cui, Y.; Dufek, E. J.; Goodenough, J. B.; Khalifah, P.; Li, Q.; Liaw, B. Y.; Liu, P.; Manthiram, A.; Meng, Y. S.; Subramanian, V. R.; Toney, M. F.; Viswanathan, V. V.; Whittingham, M. S.; Xiao, J.; Xu, W.; Yang, J.; Yang, X.-Q.; Zhang, J.-G. Pathways for Practical High-energy Long-Cycling Lithium Metal Batteries. *Nature Energy* **2019,** 4 , 180–186.
(3) Zheng, M.; Tang, H.; Hu, Q.; Zheng, S.; Li, L.; Xu, J.; Pang, H. Tungsten-Based Materials for Lithium-Ion Batteries. *Advanced Functional Materials* **2018,** *28*, 1707500.
(4) Tian, J.; Yang, Z.; Yin, Z.; Ye, Z.; Wang, J.; Cui, C.; Qian, W. Perspective to the Potential Use of Graphene in Li-ion Battery and Supercapacitor. *Chemical record* **2018**.
(5) Wei, D.; Astley, M. R.; Harris, N.; White, R.; Ryhanen, T.; Kivioja, J. Graphene Nanoarchitecture in Batteries. *Nanoscale* **2014,** *6*, 9536-9540.
(6) Guo, X.; Zheng, S.; Zhang, G.; Xiao, X.; Li, X.; Xu, Y.; Xue, H.; Pang, H. Nanostructured Graphene-Based Materials for Flexible Energy Storage. *Energy Storage Materials* **2017,** *9*, 150-169.
(7) Yang, W.; Li, X.; Li, Y.; Zhu, R.; Pang, H. Applications of Metal-Organic-Framework-Derived Carbon Materials. *Advanced materials* **2019,** *31*, e1804740.
(8) Chen, Z.; Li, H.; Wu, L.; Lu, X.; Zhang, X. $Li_4Ti_5O_{12}$ Anode: Structural Design from Material to Electrode and the Construction of Energy Storage Devices. *Chemical record* **2018,** *18*, 350-380.
(9) Liu, Y.; Zhao, M.; Xu, H.; Chen, J. Fabrication of Continuous Conductive Network for $Li_4Ti_5O_{12}$ Anode by Cu-doping and Graphene Wrapping to Boost Lithium Storage. *Journal of*

Alloys and Compounds **2019,** *780*, 1-7.
(10) Odziomek, M.; Chaput, F.; Rutkowska, A.; Swierczek, K.; Olszewska, D.; Sitarz, M.; Lerouge, F.; Parola, S. Hierarchically Structured Lithium Titanate for Ultrafast Charging in Long-Life High Capacity Batteries. *Nature communications* **2017,** *8*, 15636.
(11) Yuan, T.; Tan, Z.; Ma, C.; Yang, J.; Ma, Z.-F.; Zheng, S. Challenges of Spinel $Li_4Ti_5O_{12}$ for Lithium-Ion Battery Industrial Applications. *Advanced Energy Materials* **2017,** *7*, 1601625.
(12) Choi, J. H.; Ryu, W. H.; Park, K.; Jo, J. D.; Jo, S. M.; Lim, D. S.; Kim, I. D. Multi-Layer Electrode with Nano- $Li_4Ti_5O_{12}$ Aggregates Sandwiched between Carbon Nanotube and Graphene Networks for High Power Li-ion Batteries. *Scientific reports* **2014,** *4*, 7334.
(13) Li, F.; Zeng, M.; Li, J.; Tong, X.; Xu, H. Sb Doped $Li_4Ti_5O_{12}$ Hollow Spheres with Enhanced Lithium Storage Capability. *RSC Advances* **2016,** *6*, 26902-26907.
(14) Ming, H.; Ming, J.; Li, X.; Zhou, Q.; Wang, H.; Jin, L.; Fu, Y.; Adkins, J.; Zheng, J. Hierarchical $Li_4Ti_5O_{12}$ Particles Co-Modified with C&N Towards Enhanced Performance in Lithium-Ion battery Applications. *Electrochimica Acta* **2014,** *116*, 224-229.
(15) Park, H.; Song, T.; Han, H.; Paik, U. Electrospun $Li_4Ti_5O_{12}$ Nanofibers Sheathed with Conductive TiN/TiO_xN_y Layer as an Anode Material for High Power Li-ion Batteries. *Journal of Power Sources* **2013,** *244*, 726-730.
(16) Pohjalainen, E.; Rauhala, T.; Valkeapää, M.; Kallioinen, J.; Kallio, T. Effect of $Li_4Ti_5O_{12}$ Particle Size on the Performance of Lithium Ion Battery Electrodes at High C-Rates and Low Temperatures. *The Journal of Physical Chemistry C* **2015,** *119*, 2277-2283.
(17) Ren, Y.; Lu, P.; Huang, X.; Ding, J.; Wang, H.; Zhou, S.; Chen, Y.; Liu, B. High Performance $Li_4Ti_5O_{12}$/CN Anode Material Promoted by Melamine–Formaldehyde Resin as Carbon–Nitrogen Precursor. *RSC Advances* **2015,** *5*, 55994-56000.
(18) Shen, Y.; Eltzholtz, J. R.; Iversen, B. B. Controlling Size, Crystallinity, and Electrochemical Performance of $Li_4Ti_5O_{12}$ Nanocrystals. *Chemistry of Materials* **2013,** *25*, 5023-5030.
(19) Dong, W.; Xu, J.; Wang, C.; Lu, Y.; Liu, X.; Wang, X.; Yuan, X.; Wang, Z.; Lin, T.; Sui, M.; Chen, I. W.; Huang, F. A Robust and Conductive Black Tin Oxide Nanostructure Makes Efficient Lithium-Ion Batteries Possible. *Advanced materials* **2017**, 29, 1700136
(20) Zheng, Y.; Zhou, T.; Zhao, X.; Pang, W. K.; Gao, H.; Li, S.; Zhou, Z.; Liu, H.; Guo, Z. Atomic Interface Engineering and Electric-Field Effect in Ultrathin Bi_2MoO_6 Nanosheets for Superior Lithium Ion Storage. *Advanced materials* ***2017***, 29, 1700396.
(21) Deng, X.; Wei, Z.; Cui, C.; Liu, Q.; Wang, C.; Ma, J. Oxygen-Deficient Anatase TiO_2@C Nanospindles with Pseudocapacitive Contribution for Enhancing Lithium Storage. *Journal of Materials Chemistry A* **2018,** *6*, 4013-4022.
(22) Kim, H. S.; Cook, J. B.; Lin, H.; Ko, J. S.; Tolbert, S. H.; Ozolins, V.; Dunn, B. Oxygen Vacancies Enhance Pseudocapacitive Charge Storage Properties of MoO_{3-x}. *Nature materials* **2017,** *16*, 454-460.
(23) Zhang, H.; Jiang, Y.; Qi, Z.; Zhong, X.; Yu, Y. Sulfur Doped Ultra-Thin Anatase TiO_2 Nanosheets/Graphene Nanocomposite for High-Performance Pseudocapacitive Sodium Storage. *Energy Storage Materials* **2018,** *12*, 37-43.
(24) Ziarati, A.; Badiei, A.; Luque, R. Black Hollow TiO_2 Nanocubes: Advanced Nanoarchitectures for Efficient Visible Light Photocatalytic Applications. *Applied Catalysis B: Environmental* **2018,** *238*, 177-183.
(25) Joseph, J.; Murdock, A. T.; Seo, D. H.; Han, Z. J.; O'Mullane, A. P.; Ostrikov, K. K. Plasma

Enabled Synthesis and Processing of Materials for Lithium-Ion Batteries. *Advanced Materials Technologies* **2018,** *3*, 1800070.
(26) Zhang, Y.; Rawat, R. S.; Fan, H. J. Plasma for Rapid Conversion Reactions and Surface Modification of Electrode Materials. *Small Methods* **2017,** *1*, 1700164.
(27) Dou, S.; Tao, L.; Wang, R.; El Hankari, S.; Chen, R.; Wang, S. Plasma-Assisted Synthesis and Surface Modification of Electrode Materials for Renewable Energy. *Advanced materials* **2018,** *30*, e1705850.
(28) Shin, J.-Y.; Joo, J. H.; Samuelis, D.; Maier, J. Oxygen-Deficient $TiO_{2-\delta}$ Nanoparticles via Hydrogen Reduction for High Rate Capability Lithium Batteries. *Chemistry of Materials* **2012,** *24*, 543-551.
(29) Tao, L.; Duan, X.; Wang, C.; Duan, X.; Wang, S. Plasma-Engineered MoS_2 Thin-Film as an Efficient Electrocatalyst for Hydrogen Evolution Reaction. *Chemical communications* **2015,** *51*, 7470-7473.
(30) Xu, L.; Jiang, Q.; Xiao, Z.; Li, X.; Huo, J.; Wang, S.; Dai, L. Plasma-Engraved Co_3O_4 Nanosheets with Oxygen Vacancies and High Surface Area for the Oxygen Evolution Reaction. *Angewandte Chemie* **2016,** *55*, 5277-5281.
(31) He, H.; Huang, D.; Pang, W.; Sun, D.; Wang, Q.; Tang, Y.; Ji, X.; Guo, Z.; Wang, H. Plasma-Induced Amorphous Shell and Deep Cation-Site S Doping Endow TiO_2 with Extraordinary Sodium Storage Performance. *Advanced materials* **2018,** *30*, e1801013.
(32) Yao, Z.; Xia, X.; Xie, D.; Wang, Y.; Zhou, C.-a.; Liu, S.; Deng, S.; Wang, X.; Tu, J. Enhancing Ultrafast Lithium Ion Storage of $Li_4Ti_5O_{12}$ by Tailored TiC/C Core/Shell Skeleton Plus Nitrogen Doping. *Advanced Functional Materials* **2018,** *28*, 1802756.
(33) Lan, C.-K.; Chuang, S.-I.; Bao, Q.; Liao, Y.-T.; Duh, J.-G. One-Step Argon/Nitrogen Binary Plasma Jet Irradiation of $Li_4Ti_5O_{12}$ for Stable High-Rate Lithium Ion Battery Anodes. *Journal of Power Sources* **2015,** *275*, 660-667.
(34) Li, X.; Lin, H. C.; Cui, W. J.; Xiao, Q.; Zhao, J. B. Fast Solution-cCombustion Synthesis of Nitrogen-Modified $Li_4Ti_5O_{12}$ Aanomaterials with Improved Electrochemical Performance. *ACS applied materials & interfaces* **2014,** *6*, 7895-7901.
(35) Wang, S.; Yang, Y.; Quan, W.; Hong, Y.; Zhang, Z.; Tang, Z.; Li, J. Ti^{3+}-Free Three-Phase $Li_4Ti_5O_{12}/TiO_2$ for High-Rate Lithium Ion Batteries: Capacity and Conductivity Enhancement by Phase Boundaries. *Nano Energy* **2017,** *32*, 294-301.
(36) Zhang, G.; Xiong, T.; Yan, M.; He, L.; Liao, X.; He, C.; Yin, C.; Zhang, H.; Mai, L. α-MoO_{3-x} by Plasma Etching with Improved Capacity and Stabilized Structure for Lithium Storage. *Nano Energy* **2018,** *49*, 555-563.
(37) Li, J.; Yuan, X.; Lin, C.; Yang, Y.; Xu, L.; Du, X.; Xie, J.; Lin, J.; Sun, J. Achieving High Pseudocapacitance of 2D Titanium Carbide (MXene) by Cation Intercalation and Surface Modification. *Advanced Energy Materials* **2017,** *7*, 1602725.
(38) Lu, M.; Han, W.; Li, H.; Shi, W.; Wang, J.; Zhang, B.; Zhou, Y.; Li, H.; Zhang, W.; Zheng, W. Tent-Pitching-Inspired High-Valence Period 3-Cation Pre-Intercalation Excels for Anode of 2D Titanium Carbide (MXene) with High Li Storage Capacity. *Energy Storage Materials* **2019,** *16*, 163-168.
(39) Xia, Y.; Mathis, T. S.; Zhao, M. Q.; Anasori, B.; Dang, A.; Zhou, Z.; Cho, H.; Gogotsi, Y.; Yang, S. Thickness-Independent Capacitance of Vertically Aligned Liquid-Crystalline MXenes. *Nature* **2018,** *557*, 409-412.

(40) Xu, Y.; Zhou, M.; Zhang, C.; Wang, C.; Liang, L.; Fang, Y.; Wu, M.; Cheng, L.; Lei, Y. Oxygen Vacancies: Effective Strategy to Boost Sodium Storage of Amorphous Electrode Materials. *Nano Energy* **2017,** *38*, 304-312.

(41) Xu, Y.; Zhou, M.; Wang, X.; Wang, C.; Liang, L.; Grote, F.; Wu, M.; Mi, Y.; Lei, Y. Enhancement of Sodium Ion Battery Performance Enabled by Oxygen Vacancies. *Angewandte Chemie* **2015,** *54*, 8768-8771.

(42) Bao, J.; Zhang, X.; Fan, B.; Zhang, J.; Zhou, M.; Yang, W.; Hu, X.; Wang, H.; Pan, B.; Xie, Y. Ultrathin Spinel-Structured Nanosheets Rich in Oxygen Deficiencies for Enhanced Electrocatalytic Water Oxidation. *Angewandte Chemie* **2015,** *54*, 7399-7404.

(43) Chen, C.; Huang, Y.; An, C.; Zhang, H.; Wang, Y.; Jiao, L.; Yuan, H. Copper-Doped Dual Phase $Li_4Ti_5O_{12}$-TiO_2 Nanosheets as High-Rate and Long Cycle Life Anodes for High-Power Lithium-Ion Batteries. *ChemSusChem* **2015,** *8*, 114-122.

(44) Gan, Q.; He, H.; Zhao, K.; He, Z.; Liu, S.; Yang, S. Plasma-Induced Oxygen Vacancies in Urchin-Like Anatase Titania Coated by Carbon for Excellent Sodium-Ion Battery Anodes. *ACS applied materials & interfaces* **2018,** *10*, 7031-7042.

(45) Guo, Q.; Cheng, X.; Shi, Y.; Sheng, Z.; Chang, C. Bluish $Li_4Ti_5O_{12}$ with Enhanced Rate Performance. *Journal of Alloys and Compounds* **2017,** *710*, 383-392.

(46) Zhang, Y.; Ding, Z.; Foster, C. W.; Banks, C. E.; Qiu, X.; Ji, X. Oxygen Vacancies Evoked Blue TiO_2(B) Nanobelts with Efficiency Enhancement in Sodium Storage Behaviors. *Advanced Functional Materials* **2017,** *27*, 1700856.

(47) Li, L.; Li, G.; Xu, J.; Zheng, J.; Tong, W.; Hu, W. Insights into the Roles of Organic Coating in Tuning the Defect Chemistry of Monodisperse TiO_2 Nanocrystals for Tailored Properties. *Physical chemistry chemical physics : PCCP* **2010,** *12*, 10857-10864.

(48) Guo, M.; Chen, H.; Wang, S.; Dai, S.; Ding, L.-X.; Wang, H. TiN-Coated Micron-Sized Tantalum-Doped $Li_4Ti_5O_{12}$ with Enhanced Anodic Performance for Lithium-Ion Batteries. *Journal of Alloys and Compounds* **2016,** *687*, 746-753.

(49) Liao, J.-Y.; Chabot, V.; Gu, M.; Wang, C.; Xiao, X.; Chen, Z. Dual Phase $Li_4Ti_5O_{12}$–TiO_2 Nanowire Arrays as Integrated Anodes for High-Rate Lithium-Ion Batteries. *Nano Energy* **2014,** *9*, 383-391.

(50) Huang, C.; Zhao, S.-X.; Peng, H.; Lin, Y.-H.; Nan, C.-W.; Cao, G.-Z. Hierarchical Porous $Li_4Ti_5O_{12}$–TiO_2 Composite Anode Materials with Pseudocapacitive Effect for High-Rate and Low-Temperature Applications. *Journal of Materials Chemistry A* **2018,** *6*, 14339-14351.

(51) Luo, S.; Zhang, P.; Yuan, T.; Ruan, J.; Peng, C.; Pang, Y.; Sun, H.; Yang, J.; Zheng, S. Molecular Self-Assembly of A Nanorod N- $Li_4Ti_5O_{12}$/TiO_2/C Anode for Superior Lithium Ion Storage. *Journal of Materials Chemistry A* **2018,** *6*, 15755-15761.

(52) Hahn, B. P.; Long, J. W.; Mansour, A. N.; Pettigrew, K. A.; Osofsky, M. S.; Rolison, D. R. Electrochemical Li-Ion Storage in Defect Spinel Iron Xxides: the Critical Role of Cation Vacancies. *Energy & Environmental Science* **2011,** *4*, 1495.

(53) Li, G.; Blake, G. R.; Palstra, T. T. Vacancies in Functional Materials for Clean Energy Storage and Harvesting: the Perfect Imperfection. *Chem Soc Rev* **2017,** *46*, 1693-1706.

(54) Xu, H.; Chen, J.; Li, Y.; Guo, X.; Shen, Y.; Wang, D.; Zhang, Y.; Wang, Z. Fabrication of L $Li_4Ti_5O_{12}$-TiO_2 Nanosheets with Structural Defects as High-Rate and Long-Life Anodes for Lithium-Ion Batteries. *Scientific reports* **2017,** *7*, 2960.

(55) Xia, Q.; Jabeen, N.; Savilov, S. V.; Aldoshin, S. M.; Xia, H. Black Mesoporous $Li_4Ti_5O_{12-\delta}$

Nanowall aArrays with Improved Rate Performance as Advanced 3D Anodes for Microbatteries. *Journal of Materials Chemistry A* **2016,** *4*, 17543-17551.
(56) Qin, T.; Zhang, X.; Wang, D.; Deng, T.; Wang, H.; Liu, X.; Shi, X.; Li, Z.; Chen, H.; Meng, X.; Zhang, W.; Zheng, W. Oxygen Vacancies Boost delta-Bi_2O_3 as a High-Performance Electrode for Rechargeable Aqueous Batteries. *ACS applied materials & interfaces* **2019,** *11*, 2103-2111.
(57) Feng, X.-Y.; Li, X.; Tang, M.; Gan, A.; Hu, Y.-Y. Enhanced Rate Performance of $Li_4Ti_5O_{12}$ Anodes with Bridged Grain Boundaries. *Journal of Power Sources* **2017,** *354*, 172-178.
(58) Yang, Z.; Huang, Q.; Li, S.; Mao, J. High-Temperature Effect on Electrochemical Performance of $Li_4Ti_5O_{12}$ Based Anode Material for Li-Ion Batteries. *Journal of Alloys and Compounds* **2018,** *753*, 192-202.
(59) Chen, C.; Xu, H.; Zhou, T.; Guo, Z.; Chen, L.; Yan, M.; Mai, L.; Hu, P.; Cheng, S.; Huang, Y.; Xie, J. Integrated Intercalation-Based and Interfacial Sodium Storage in Graphene-Wrapped Porous $Li_4Ti_5O_{12}$ Nanofibers Composite Aerogel. *Advanced Energy Materials* **2016,** *6*, 1600322.
(60) Wu, Q.; Xu, J.; Yang, X.; Lu, F.; He, S.; Yang, J.; Fan, H. J.; Wu, M. Ultrathin Anatase TiO2Nanosheets Embedded with TiO_2-B Nanodomains for Lithium-Ion Storage: Capacity Enhancement by Phase Boundaries. *Advanced Energy Materials* **2015,** *5*, 1401756.
(61) Zhang, Q.; Yan, Y.; Chen, G. A Biomineralization Strategy for "Net"-Like Interconnected TiO_2 Nanoparticles Conformably Covering Reduced Graphene Oxide with Reversible Interfacial Lithium Storage. *Advanced science* **2015,** *2*, 1500176.
(62) Ma, J.; Wei, Y.; Gan, L.; Wang, C.; Xia, H.; Lv, W.; Li, J.; Li, B.; Yang, Q.-H.; Kang, F.; He, Y.-B. Abundant Grain Boundaries Activate Highly Efficient Lithium Ion Transportation in High Rate $Li_4Ti_5O_{12}$ Compact Microspheres. *Journal of Materials Chemistry A* **2019**,**7**, 1168-1176
(63) Xu, G.; Tian, Y.; Wei, X.; Yang, L.; Chu, P. K. Free-Standing Electrodes Composed of Carbon-Coated $Li_4Ti_5O_{12}$ Nanosheets and Reduced Graphene Oxide for Advanced Sodium Ion Batteries. *Journal of Power Sources* **2017,** *337*, 180-188.
(64) Hong, Z.; Zhou, K.; Huang, Z.; Wei, M. Iso-Oriented Anatase TiO_2 Mesocages as a High Performance Anode Material for Sodium-Ion Storage. *Scientific reports* **2015,** *5*, 11960.
(65) Hou, C.; Hou, Y.; Fan, Y.; Zhai, Y.; Wang, Y.; Sun, Z.; Fan, R.; Dang, F.; Wang, J. Oxygen Vacancy Derived Local Build-in Electric Field in Mesoporous Hollow Co_3O_4 Microspheres Promotes High-Performance Li-Ion Batteries. *Journal of Materials Chemistry A* **2018,** *6*, 6967-6976.
(66) Yan, B.; Li, M.; Li, X.; Bai, Z.; Yang, J.; Xiong, D.; Li, D. Novel Understanding of Carbothermal Reduction Enhancing Electronic and Ionic Conductivity of $Li_4Ti_5O_{12}$ Anode. *Journal of Materials Chemistry A* **2015,** *3*, 11773-11781.
(67) Zhang, Y.; Luo, Y.; Chen, Y.; Lu, T.; Yan, L.; Cui, X.; Xie, J. Enhanced Rate Capability and Low-Temperature Performance of $Li_4Ti_5O_{12}$ Anode Material by Facile Surface Fluorination. *ACS applied materials & interfaces* **2017,** *9*, 17145-17154.
(68) Kim, M.-C.; Moon, S.-H.; Han, S.-B.; Kwak, D.-H.; Lee, J.-E.; Kim, E.-S.; Choi, S.; Shin, Y.-K.; Park, K.-W. Sea Urchin-Like $Li_4Ti_5O_{12}$ Nanostructure as a Li-Ion Battery Anode with High Energy Density and Improved Ionic Transport. *Journal of Alloys and Compounds* **2018,** *767*, 73-80.
(69) Li, Z.; Ding, F.; Zhao, Y.; Wang, Y.; Li, J.; Yang, K.; Gao, F. Synthesis and Electrochemical Performance of $Li_4Ti_5O_{12}$ Submicrospheres Coated with TiN as Anode Materials for Lithium-Ion Battery. *Ceramics International* **2016,** *42*, 15464-15470.

(70) Ventosa, E.; Xia, W.; Klink, S.; La Mantia, F.; Mei, B.; Muhler, M.; Schuhmann, W. Ammonia-Annealed TiO_2 as a Negative Electrode material in li-ion batteries: N doping or oxygen deficiency? *Chemistry* **2013,** *19*, 14194-14199.
(71) Sha, Y.; Xu, X.; Li, L.; Cai, R.; Shao, Z. Hierarchical Carbon-Coated Acanthosphere-Like $Li_4Ti_5O_{12}$ Microspheres for High-Power Lithium-Ion Batteries. *Journal of Power Sources* **2016,** *314*, 18-27.
(72) Sun, L.; Wang, J.; Jiang, K.; Fan, S. Mesoporous $Li_4Ti_5O_{12}$ Nanoclusters as High Performance Negative Electrodes for Lithium Ion Batteries. *Journal of Power Sources* **2014,** *248*, 265-272.
(73) Wang, C.; Wang, S.; He, Y.-B.; Tang, L.; Han, C.; Yang, C.; Wagemaker, M.; Li, B.; Yang, Q.-H.; Kim, J.-K.; Kang, F. Combining Fast Li-Ion Battery Cycling with Large Volumetric Energy Density: Grain Boundary Induced High Electronic and Ionic Conductivity in $Li_4Ti_5O_{12}$ Spheres of Densely Packed Nanocrystallites. *Chemistry of Materials* **2015,** *27*, 5647-5656.
(74) He, Y.; Muhetaer, A.; Li, J.; Wang, F.; Liu, C.; Li, Q.; Xu, D. Ultrathin $Li_4Ti_5O_{12}$ Nanosheet Based Hierarchical Microspheres for High-Rate and Long-Cycle Life Li-Ion Batteries. *Advanced Energy Materials* **2017,** *7*, 1700950.
(75) Li, X.; Wei, J.; Li, Q.; Zheng, S.; Xu, Y.; Du, P.; Chen, C.; Zhao, J.; Xue, H.; Xu, Q.; Pang, H. Nitrogen-Doped Cobalt Oxide Nanostructures Derived from Cobalt-Alanine Complexes for High-Performance Oxygen Evolution Reactions. *Advanced Functional Materials* **2018,** *28*, 1800886.
(76) Cheng, F.; Zhang, T.; Zhang, Y.; Du, J.; Han, X.; Chen, J. Enhancing Electrocatalytic Oxygen Reduction on MnO_2 with Vacancies. *Angewandte Chemie* **2013,** *52*, 2474-2477.
(77) Sadighi, Z.; Huang, J.; Qin, L.; Yao, S.; Cui, J.; Kim, J.-K. Positive Role of Oxygen Vacancy in Electrochemical Performance of $CoMn_2O_4$ Cathodes for Li-O_2 Batteries. *Journal of Power Sources* **2017,** *365*, 134-147.

TOC

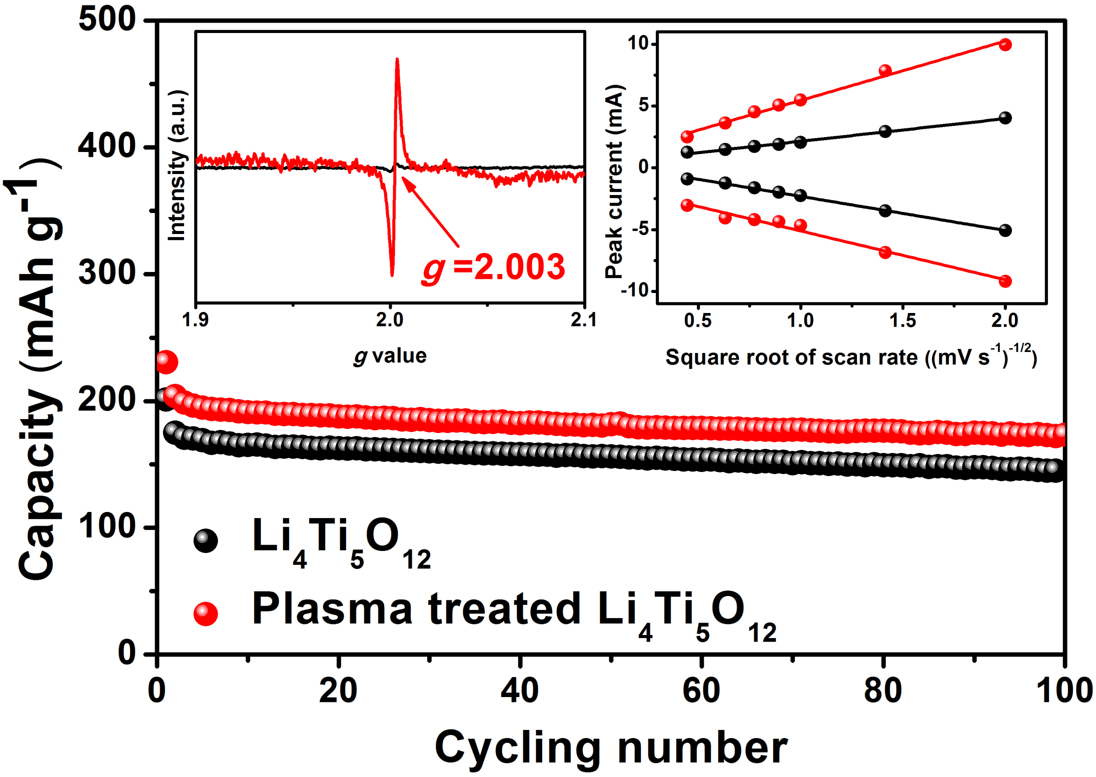

Capacity (mAh g-1)
Cycling number
Intensity (a.u.)
g value
g =2.003
Peak current (mA)
Square root of scan rate ((mV s-1)-1/2)
Li4Ti5O12
Plasma treated Li4Ti5O12